

Size matters: The rotation rates of small near-Earth asteroids

Thomas S. Statler^{a,b,*}, Desireé Cotto-Figueroa^a, David A. Riethmiller^a, Kevin M. Sweeney^a

^a Astrophysical Institute, Department of Physics and Astronomy, 251B Clippinger Research Laboratories, Ohio University, Athens, OH 45701, USA

^b Division of Astronomical Sciences, National Science Foundation, 4201 Wilson Blvd., Arlington, VA 22230, USA

ARTICLE INFO

Article history:

Received 13 June 2012

Revised 23 February 2013

Accepted 15 March 2013

Available online 30 March 2013

Keywords:

Asteroids, Dynamics

Asteroids, Rotation

Asteroids, Surfaces

Near-Earth objects

ABSTRACT

We present results from a program of optical light curve observations of near-Earth asteroids (NEAs) with diameters under 1 km, designed to detect, and determine the distribution of, rotation periods shorter than a few hours. We obtain measurements or estimates of rotation period P for approximately one third of the 83 NEAs observed. Most of the measured periods are in the fast-rotating asteroid (FRA) regime ($P < 2$ h). We assess our detection sensitivity using simulated light curves and a new Monte Carlo algorithm (SALSA), which allows us to de-bias the counts of detected FRAs and determine the fraction of objects that are fast rotators as a function of H . We find that the FRA fraction F rises sharply from zero to a value statistically consistent with unity from $H = 21.4$ to $H = 23.6$, a span corresponding to a factor of only 2.8 in nominal diameter. Almost nothing larger than 170 m, and almost everything smaller than 60 m, is a fast rotator, assuming a mean S class albedo of 0.17. The formal 95% confidence limits are $F < 13\%$ for $18.5 < H < 21.4$ and $F > 56\%$ for $23.6 < H < 26.3$. Relative to a distribution with the same FRA fraction that is uniform in frequency (as implied by models of evolution following the YORP cycle) up to a size-dependent upper cutoff, the actual spin distribution extends to shorter periods. Approximately two thirds of our sample shows ambiguous light curves from which no period estimate can be obtained. Finite photometric errors account for some of these, but do not explain the steep increase in the ambiguous fraction toward larger objects, which suggests an increase in the actual fraction of very slow rotators, very fast rotators, or nearly axisymmetric objects. With a significantly larger data set, our fully general SALSA procedure will be able to extract the NEA spin rate distribution as a function of absolute magnitude H . Determining this distribution to the accuracy needed to constrain the physical properties of NEAs and their dynamical evolution will require larger samples, and homogeneous, unbiased reporting of the data, including accurate errors, for all objects observed, not just those with measured periods.

© 2013 Elsevier Inc. All rights reserved.

1. Introduction

The distribution of rotation rates as a function of size is one of the key lines of evidence indicating that most asteroids are not monolithic. For large objects, this distribution shows a remarkably sharp upper limit, corresponding to periods near 2 h. As this is close to the dynamical time $(G\rho)^{-1/2}$ for densities ρ of stony meteorites, the limit has been universally interpreted as an indication that asteroids larger than a few hundred meters in size are gravitational aggregates—or, more colloquially, “rubble piles” (Harris, 1996).

Since 1996, a population of small objects (nominal diameters <150 m) with rotation periods under 2 h has been identified, in increasing numbers. These objects were initially designated “monolithic fast-rotating asteroids” (Whiteley et al., 2000), a name

that implies a distinction between, on the one hand, large, slowly rotating objects that have been fractured by impacts, or shattered and reassembled, and, on the other, small, fast rotators that have the tensile strength of solid rock. The legitimacy of the distinction, however, is far from clear. While large objects are dominated by self-gravity with friction contributing to the rigidity, small objects may be strength-dominated and still not monolithic. A weakly cohesive aggregate of small particles can have sufficient strength to hold together at rotation rates as fast as those observed (Holsapple, 2007). Thus the purely empirical term “fast-rotating asteroids” (FRAs) is much more appropriate.

Weak binding, whether gravitational or material, renders objects susceptible to reconfiguration or dissociation by impacts, tidal encounters, or secular torques. For near-Earth asteroids (NEAs) smaller than a few km in size, the dominant torque is the YORP effect, arising from radiation recoil integrated over the asymmetric surface. YORP affects both spin rate and obliquity, in an obliquity-dependent way; obliquity and spin thus evolve together over time. In the classical “YORP cycle” (Bottke et al., 2006, and references therein), a typical object goes through a period of

* Corresponding author at: Astrophysical Institute, Department of Physics and Astronomy, 251B Clippinger Research Laboratories, Ohio University, Athens, OH 45701, USA. Fax: +1 740 593 0433.

E-mail address: statler@ohio.edu (T.S. Statler).

rotational acceleration, then deceleration, evolving toward an asymptotically stable obliquity, and eventually settling into slow tumbling before being randomly reoriented to an obliquity that initiates a new cycle. Simulations (Rossi et al., 2009) imply that individual NEAs can go through tens of YORP cycles, or more, during their lifetimes, meaning that YORP could have rewritten the NEA spin state distribution many times over and erased all memory of the initial obliquity with which these objects arrived in the inner Solar System. This would seem inconsistent with the finding (Chesley et al., 2008) that small NEAs with measurable semi-major axis drifts due to the Yarkovsky effect are overwhelmingly drifting inward, implying retrograde rotation, as expected for NEAs newly arrived from the Main Belt. But the simple picture of the YORP cycle assumes the object is rigid, and ignores internal reconfigurations, or movements or losses of surface material, that can result from increasing—or decreasing—spin. Even small changes of this sort can alter the YORP torque by factors of order unity (Statler, 2009; Scheeres and Gaskell, 2008). Statler (2009) suggests that non-monoolithic objects may random-walk up and down in spin rate, with torque reversals driven by stochastic movement of material rather than by smooth evolution through the YORP cycle.

Exactly how an aggregate object will reconfigure itself as centrifugal forces change depends on the nature of the aggregate (i.e., many small pieces or a few big chunks) as well as on the binding forces (gravity, cohesion, and/or friction). Numerical experiments show that idealized, self-gravitating cohesionless aggregates of a few thousand particles, subjected to a monotonically accelerating spin, gradually become axisymmetric before shedding material from the equator (Walsh et al., 2008). A “contact binary” made of two large components, similarly spun up, can pass through a sequence of progressively more elongated resting configurations before the bodies lose contact (Scheeres, 2007). Either way, YORP acceleration may cause the dissociation of some loosely bound gravitational aggregates. The fact that NEA binaries nearly all have rapidly rotating primaries (Richardson and Walsh, 2006) suggests that YORP may be a factor in their formation. But one should not assume that monotonic spin-up to a binary-forming threshold is guaranteed, considering the extreme sensitivity of YORP to small internal or surface reconfigurations.

The FRAs are rotating under centrifugal tension, and are strength-dominated rather than gravity-dominated. For these objects, the envelope of maximum spin rate as a function of size is a gauge of material properties—particularly cohesive forces—that are obscured by self-gravity in larger bodies. The detailed FRA spin distribution is a constraint on evolutionary models, a clue to the relative roles of the YORP cycle vs. random-walk spin evolution, and a consistency check on the distribution of Yarkovsky drift rates. Models of quasi-continuous cohesive aggregates predict a gradual increase in the maximum sustainable spin rate with decreasing size (Holsapple, 2005). But observations to date have not revealed the expected moderately-fast rotators in the transition region below approximately 1 km (e.g. Pravec et al., 2005).

Existing rotation data are extremely heterogeneous. The great majority of period measurements are derived from optical light curves obtained by both professional observers and dedicated amateurs. Most of the photometric data are not published, and of those, a significant fraction lack error estimates. Selection biases are unquantifiable, and, along with reporting bias—the tendency not to report observations that do not result in measured periods—make the available data poorly suited to addressing statistical questions about the spin rate distribution. Turning counts of measured periods into actual distributions of spin rates requires statistical correction for the objects that are not detected due to unfavorable geometry, observational errors, or both. The absence

of photometric errors and data for non-detections in the database makes this correction impossible.

In this paper we present results from a light curve survey of 83 sub-kilometer-sized NEAs. Our survey is comparable in scale to the recent work of Hergenrother and Whiteley (2011, hereafter HW), though our sample extends to larger objects than does HW’s. The primary difference between our work and previous studies is that we correct for observational incompleteness using an extensive set of Monte Carlo simulations, debiasing the raw counts in order to obtain statistically rigorous constraints on the fraction of fast rotators as a function of size, including confidence limits. Section 2 below describes our observational strategy, data acquisition and reduction methods, and the resulting light curves and rotation period measurements. Section 3 then takes up the issue of observational sensitivity and incompleteness, and presents a completely general method that will be able to extract the full spin rate distribution as a function of absolute magnitude when a sufficiently large sample with well-characterized errors becomes available. In Section 4 we use this approach with our data to obtain the debiased fraction of fast rotators as a function of absolute magnitude. Section 5 discusses the interpretation and implications of our main results. Finally, Section 6 sums up the conclusions and highlights prospects and strategies for future work.

2. Rotation period measurements

2.1. Observations

Between 2006 and 2010, we observed 83 NEAs using the 2.4-m Hiltner telescope at the MDM Observatory on Kitt Peak. Targets were chosen each afternoon using the Minor Planet Center’s NEO Confirmation List, the ESA Spaceguard System’s Priority list, and, later in the program, the NEO Dynamics Site’s search utility. Targets were required to lie north of $\delta = -5^\circ$, to have absolute magnitudes $H > 18$ and apparent magnitudes $V < 20$, and proper motions $< 5^\circ \text{ day}^{-1}$. Initially, the emphasis was on searching for FRAs in the transition region $21.5 > H > 17$ corresponding to nominal diameters between about 150 m and 1 km. Later in the program, as it became apparent that the transition region is largely devoid of fast rotators, we simply targeted the smallest objects observable each night. Objects fainter than $V = 19.5$ were observed only in seeing of 1 arcsec or better, which occurred infrequently.

Table 1 lists the basic physical (H) and orbital parameters (a , e , and i) for the observed NEAs, obtained from the JPL Small-Body Database, as well as the observational circumstances (date, apparent V magnitude, and phase angle) for each object, from NEODyS. Objects in the sample have absolute magnitudes in the range $18.3 \leq H \leq 26.3$, corresponding to nominal diameters of approximately 700–20 m assuming (as we will throughout this paper) a mean S-class albedo of 0.17 (Mainzer et al., 2011b).

The project was conducted as a *bright time* program, and observations were made in a variety of sky conditions ranging from patchy clouds to thin cirrus to (on rare occasions) photometric. All imaging was done in R band, to reduce the sky brightness relative to the expected red colors of the asteroids. The detector for nearly all observations was the SITE CCD “Echelle”, with a plate scale of $0.28'' \text{ pix}^{-1}$. For the 2010 October run we used the “Templeton” CCD, a smaller detector having the same plate scale and same manufacturer as Echelle. Our observing procedures evolved early in the program, but after the first two runs, we settled on the following strategy. Objects were imaged using a 1200×1200 pixel subframe of the CCD, giving a roughly 5 arcmin square field, as a compromise between the CCD’s slow readout time and the need for a good number of comparison stars. Because accurate bright sky subtraction requires accurate knowledge of the wings of the point spread

Table 1
Near-Earth asteroids observed.

Name	<i>a</i>	<i>e</i>	<i>i</i>	<i>H</i>	Date	<i>V</i>	Phase	$\langle \sigma_{\text{stat phot}}^2 \rangle$
2006 CL ₉	1.346	0.2367	2.935	22.7	2006/02/11.20–11.32	18.1	38.7	0.047
2006 CN ₁₀	2.800	0.6075	1.237	21.0	2006/02/11.34–11.44	18.6	8.5	0.028
2006 CY ₁₀	1.959	0.4860	6.785	20.3	2006/02/11.48–11.56	19.0	40.6	0.042
2005 YT ₅₅	2.254	0.4585	2.299	20.6	2006/02/13.20–13.41	18.7	11.5	0.071
2006 CL ₁₀	1.707	0.4453	7.668	21.1	2006/02/13.46–13.55	19.4	70.9	0.244
2006 BN ₅₅	1.871	0.5543	18.675	19.8	2006/02/15.23–15.42	18.8	27.6	0.043
2006 UQ ₁₇	1.624	0.3808	1.744	21.9	2006/12/31.19–31.36	15.8	38.9	0.020
2006 PA ₁	2.034	0.5504	2.433	19.7	2006/12/31.37–31.56	17.5	42.3	0.012
2006 WU ₂₉	2.622	0.5260	28.913	18.3	2007/01/01.08–01.25	18.4	41.0	0.030
2006 UN ₂₁₆	3.206	0.6188	11.855	18.9	2007/01/02.17–02.34	17.1	14.9	0.014
2006 YU ₁	2.652	0.5506	8.148	20.9	2007/01/02.35–02.51	18.7	13.2	0.051
2007 DB ₆₁	0.811	0.3649	5.383	23.4	2007/03/06.12–06.29	19.2	34.5	0.061
2007 CQ ₅	1.541	0.2879	4.644	22.1	2007/03/06.38–06.55	19.5	34.0	0.032
2007 DW	1.079	0.5247	38.694	20.3	2007/03/07.11–07.20	20.0	51.8	0.077
2007 DD	0.989	0.1156	2.6217	25.8	2007/03/07.21–07.37	19.9	20.6	0.085
2006 VC	1.942	0.4918	12.256	19.9	2007/03/08.46–08.55	20.0	40.7	0.041
2006 VD ₁₃	1.948	0.4840	11.713	19.0	2007/03/09.10–09.25	17.6	50.0	0.013
2007 CO ₂₆	2.798	0.6097	7.112	21.3	2007/03/09.28–09.44	17.8	9.0	0.013
2007 DD ₄₉	0.989	0.1156	2.622	18.9	2007/03/10.11–10.17	19.5	41.9	0.045
2007 DF ₈	1.821	0.4538	9.103	20.3	2007/03/10.18–10.33	19.8	33.2	0.033
2007 AH ₁₂	2.043	0.4531	10.453	20.5	2007/03/10.35–10.50	19.3	27.5	0.024
2007 DY ₄₀	1.718	0.5917	5.879	20.8	2007/03/11.17–11.33	20.0	8.5	0.147
2007 DS ₈₄	1.866	0.4467	8.914	20.8	2007/03/11.34–11.50	18.6	45.1	0.014
2007 EF	0.820	0.4101	21.735	21.4	2007/03/12.10–12.18	19.3	85.9	0.157
2007 EV	1.091	0.3080	8.179	25.0	2007/03/12.21–12.37	19.1	37.6	0.111
2007 EQ	1.629	0.4476	5.668	21.1	2007/03/12.38–12.43	18.6	44.3	0.018
2007 WF ₅₅	2.400	0.5278	19.681	19.1	2008/01/26.10–26.16	20.3	25.6	0.115
2008 AF ₄	1.383	0.4108	8.920	19.7	2008/01/26.40–26.49	16.8	24.5	0.011
2007 PS ₉	1.074	0.0763	8.702	23.5	2008/01/31.27–31.42	18.8	4.3	0.103
2006 JY ₂₅	1.126	0.4792	6.871	20.4	2008/02/14.14–14.27	18.6	48.3	0.037
2008 CP	1.120	0.0778	13.592	24.0	2008/02/14.28–14.41	18.8	22.4	0.027
2008 CC ₇₁	1.454	0.3691	1.876	24.9	2008/02/14.46–14.50	17.6	15.7	0.277
2007 TU ₂₄	2.043	0.5343	5.622	20.3	2008/02/14.52–14.56	16.6	32.2	0.008
2008 CR ₁₁₆	1.470	0.2676	30.090	20.5	2008/02/18.38–18.54	17.4	23.8	0.045
2008 UE ₇	1.648	0.4480	3.951	20.4	2008/11/11.27–11.45	18.6	21.1	0.032
2008 VU ₃	2.485	0.6199	3.937	23.3	2008/11/11.47–11.54	19.1	32.2	0.039
2008 US ₄	2.333	0.6343	13.198	20.9	2008/11/12.07–12.22	17.5	65.4	0.082
2007 AE ₁₂	1.685	0.5694	2.285	19.2	2008/11/12.39–12.54	17.5	50.4	0.010
2008 TK ₁₅₇	2.391	0.5158	4.544	20.6	2008/11/13.21–13.33	19.1	21.1	0.089
2008 VF	0.906	0.3259	26.200	19.4	2008/11/13.34–13.53	18.4	34.9	0.067
2008 SX ₇	2.436	0.4835	6.489	18.4	2008/11/14.06–14.21	19.9	46.9	0.070
2008 SN ₁	2.662	0.5119	6.050	19.6	2008/11/14.23–14.36	19.5	14.4	0.081
2008 TQ ₂	1.845	0.4201	3.878	20.9	2008/11/14.45–14.55	19.9	48	0.104
2008 UN ₉₀	1.405	0.1257	17.545	19.9	2008/11/15.07–15.21	20.1	37.8	0.332
2008 SE	2.360	0.4860	8.629	19.4	2008/11/15.24–15.40	18.1	8.3	0.051
2008 SV ₇	1.626	0.3314	4.420	21.5	2008/11/15.41–15.55	19.8	44	0.166
2008 SH ₈₂	2.441	0.5914	4.567	21.4	2008/11/16.07–16.20	20.1	72.2	0.174
2008 VH ₁₄	2.849	0.6463	1.430	23.6	2008/11/16.21–16.31	20.0	4.1	0.115
2008 UT ₅	2.275	0.5540	1.611	24.5	2008/11/16.32–16.46	18.7	19.4	0.123
2009 HG ₆₀	1.985	0.6433	6.954	22.7	2009/04/30.15–30.31	18.0	24.9	0.025
2009 HL ₂₁	1.663	0.4444	1.007	22.4	2009/04/30.32–30.44	18.8	10.5	0.017
2009 EQ ₂	2.413	0.5007	6.512	20.8	2009/04/30.45–30.49	19.2	22.9	0.019
2009 HK ₇₃	1.246	0.2826	5.626	26.3	2009/05/01.31–01.49	18.8	30.2	0.026
2009 HU ₄₄	0.830	0.6443	6.645	22.5	2009/05/04.15–04.31	19.9	23.3	0.132
2009 HM ₈₂	1.273	0.3027	20.417	22.5	2009/05/04.32–04.49	18.4	37.2	0.054
2009 UO ₃	2.454	0.5813	8.526	23.0	2009/10/30.09–30.26	18.3	37	0.080
2009 UY ₁₉	1.023	0.0308	9.054	23.4	2009/10/30.27–30.44	16.7	22	0.029
2009 RN	2.842	0.6139	3.395	19.9	2009/10/31.38–31.54	17.1	33.5	0.080
2009 UX ₈₇	1.096	0.1137	12.911	25.3	2009/11/01.08–01.25	18.7	31.4	0.244
2009 TK ₈	0.929	0.3404	21.162	20.1	2009/11/01.27–01.44	17.6	20.5	0.016
2009 UL ₂₈	2.032	0.5342	2.876	24.8	2009/11/02.27–02.43	19.5	29.4	0.162
2009 UD ₁₉	1.672	0.4176	3.573	24.0	2009/11/02.44–02.53	19.8	27.3	0.185
2009 TK ₁₂	1.696	0.5845	3.839	20.6	2009/11/03.08–03.25	18.0	18.5	0.027
2009 SV ₁₇₁	2.632	0.5898	12.985	19.6	2009/11/03.28–03.44	18.0	33.3	0.023
2009 QB ₃₅	2.284	0.5001	5.047	19.9	2009/11/03.45–03.53	19.7	45.3	0.091
2009 UM ₂₈	1.890	0.4320	8.792	23.6	2009/11/04.07–04.23	19.7	23.7	0.169
2009 UZ ₈₇	0.924	0.1879	3.777	26.0	2009/11/04.24–04.30	19.8	8.2	0.205
2009 UX ₁₇	1.189	0.0836	10.805	21.6	2009/11/04.31–04.48	18.9	5.9	0.081
2009 RD ₄	2.730	0.5980	22.500	20.5	2009/11/05.07–05.23	19.8	53.6	0.050
2009 SF ₂	2.251	0.4489	6.419	20.8	2009/11/05.42–05.53	19.7	23.5	0.086
2010 GA ₃₄	1.457	0.2986	4.292	22.5	2010/05/21.18–21.47	18.6	73.4	0.028
2010 JE ₈₈	2.109	0.7637	10.792	21.5	2010/05/22.15–22.29	19.8	23.7	0.081
2010 CL ₁₈	2.679	0.5623	18.279	18.3	2010/05/22.36–22.48	19.2	37.4	0.016

(continued on next page)

Table 1 (continued)

Name	a	e	i	H	Date	V	Phase	$\langle \sigma_{\text{stat phot}} \rangle$
2010 FC ₈₁	2.673	0.6261	1.683	21.9	2010/05/23.22–23.31	17.2	34.1	0.021
2010 JO ₇₁	1.171	0.3863	5.990	23.9	2010/05/23.34–23.47	19.5	50.6	0.146
2010 CJ ₁₇₁	1.997	0.4908	7.375	21.2	2010/05/24.14–24.23	19.9	81.6	0.131
2010 JK ₄₁	2.746	0.5682	25.495	20.1	2010/05/25.15–25.27	19.1	37	0.047
2010 KK ₃₇	1.586	0.4431	9.051	25.7	2010/05/25.27–25.48	19.2	29.2	0.044
2010 SK ₁₅	2.330	0.5554	4.750	22.8	2010/10/16.35–16.52	18.9	14.6	0.029
2010 TU ₁₄₉	2.201	0.8281	1.972	20.7	2010/10/17.30–17.46	19.3	34.4	0.028
2010 TM ₃	1.427	0.2176	8.607	20.5	2010/10/18.41–18.53	18.5	34.5	0.023
2010 TF ₅₄	3.282	0.6748	12.086	19.6	2010/10/19.08–19.16	18.5	48.8	0.187
2010 TC ₅₅	2.847	0.6201	19.855	20.2	2010/10/19.17–19.35	18.5	24.8	0.022

function (PSF), the telescope tracked at the sidereal rate and all exposures were autoguided on stars, allowing the asteroid to trail. Between exposures, the telescope was moved so as to keep the asteroid near the center of the field while the stars drifted, frame by frame, across the field. The 30 s exposure time, plus approximately 45 s for readout and 15–20 s for repositioning the telescope and other overheads gave typical maximum frame rates of 90–100 s. We intentionally avoided a uniform cadence, to ensure good phase coverage at all possible periods and minimize problems with aliasing. Often, practical needs such as acquiring new guide stars took care of this concern for us; at other times we deliberately inserted random delays between exposures approximately every 10–20 frames. Nominally, objects were observed for 4 h, in order to provide good sensitivity to periods up to 2 h (and declining sensitivity to longer periods). In practice, not all objects could be observed for that long, usually owing to weather conditions or the approach of sunrise.

2.2. Photometry

We performed basic reductions using standard procedures in IRAF. These steps consisted of overscan and bias correction and flat-fielding. Flat-fielding was done using twilight sky flats, generally taken at the beginning and end of each night. In cases where bad weather prevented nightly flats, we used flats from an adjacent night. When flat-fielding residuals were apparent, dark-sky flats derived from the full set of asteroid images were used for a second correction.

We found that standard aperture photometry techniques performed poorly on these data, especially in bright sky conditions when transparency and seeing were variable. Therefore all of the subsequent analysis was done using a suite of custom IDL procedures.

The analysis starts by manually identifying the asteroid in each frame; then an automatic procedure identifies stars free from close neighbors, rejecting cosmic rays and extended objects using a fit to an approximate PSF. Stars are matched across frames, relative pixel shifts between frames are determined, and the proper motion of the asteroid is measured precisely in detector coordinates from its total motion over the whole observation. For each frame, stellar photometry is then done by PSF fitting. This is performed in multiple steps. The first step is to separate the sky level from the extended wings of the PSF and obtain an accurate measurement of the former. Each stellar image is fitted using an elliptical Moffatt profile and a constant sky value. Multiple fits are done, varying the Moffatt β parameter describing the slope of the PSF wings. We check for correlation between the fitted sky value around each star and the stellar flux, and choose a single β value for the entire observation window which best eliminates any correlation across all frames. The sky brightness, which may still be position-dependent across the frame, is fixed for each star for the subsequent steps. Next, each star is re-fitted using an

elliptical Gaussian, or, when the signal-to-noise ratio is high enough, a sum of two elliptical Gaussians; the latter fit is adopted if it improves the reduced χ^2 . A mean PSF is then determined for the frame, from an average of the stellar fits. A stringent rejection is applied as a second filter against extended objects or blends of multiple stellar images. Finally, the flux of each star is determined by fitting the adopted mean PSF within a circle of radius 3 times the Gaussian σ of the PSF core. For the asteroid, the mean PSF is convolved with the asteroid's known motion across the detector to produce a trailed PSF. Fitting the trailed PSF to the asteroid image, with the sky determined in a separate initial step, as above, then yields the asteroid flux. We estimate photometric errors for all objects by Monte Carlo bootstrapping, using 100 simulated images of each object derived from the fitted parameters. The bootstrap ensures that the statistical errors are properly estimated in spite of the multi-step nature of the fitting procedure.

As our main goal is to measure the distribution of spin rates, we have not observed photometric standards and we are not striving for absolute calibration. All magnitudes reported in this paper are in *instrumental R band*. Even so, relative flux calibration is still non-trivial. Because the asteroid's motion usually spans several fields over the course of an observation, we have a continually changing, but overlapping, set of comparison stars. With the photometry properly calibrated, the magnitudes of these stars should remain constant, to within the errors, for whatever span of time they are observed. We therefore use an optimization procedure that computes an additive zeropoint shift (in magnitudes) for each frame so as to minimize the weighted mean variation of all stars about their mean values. The standard deviation of the calibrated stellar magnitudes about their means is taken to be the statistical error in the zeropoint, which is added in quadrature to the bootstrapped error computed for the asteroid to yield a total statistical error for the asteroid magnitude in each frame. The upper solid histogram in Fig. 1 shows the distribution of errors for the entire data set; the median error is 0.038 mag. The unweighted mean error for each object is given in the last column of Table 1.

We have also corrected for possible slow drifts in zeropoint due to small residual errors in flat-fielding and/or field illumination. A spurious net gradient in the flat field can make it appear as if stars are systematically brightening or dimming as they drift across the field from frame to frame, an effect indistinguishable from a gradual change in atmospheric transparency. When removed in the calibration stage, this spurious trend would be imposed (in reverse) on the light curve of the asteroid, which would not suffer the same systematic dimming or brightening trend in the raw photometry since it is kept near the center of the field. When we search for periodicities (see below), we simultaneously fit a linear trend to the light curve, to remove this effect to the extent possible. All of the folded light curves shown in this paper have been de-trended.

Fig. 2a shows the fully reduced and de-trended (but not folded) light curve of 2006 CL₉. This example highlights the typical hall-

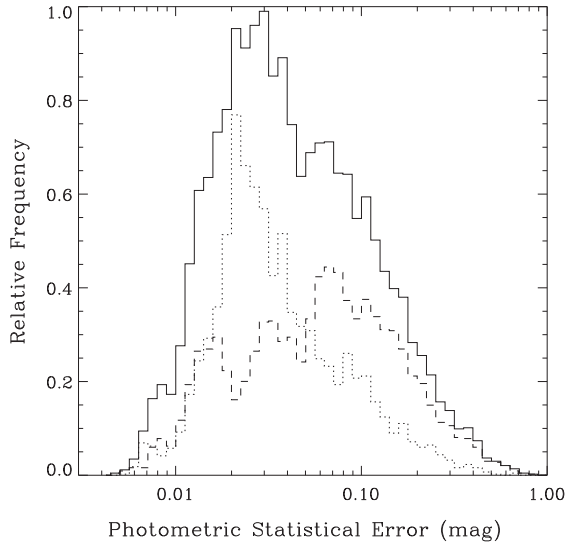


Fig. 1. Solid line: Distribution of statistical photometric errors for all asteroid flux measurements, in magnitudes; the median error is 0.038 mag. Dotted line: Same, for objects with period measurements, estimates, or upper limits; the median is 0.030 mag. Dashed line: Same, for objects with ambiguous or featureless light curves; the median is 0.062 mag.

marks of a fast rotator visible in the raw data: rapid frame-to-frame brightness variations well in excess of the statistical errors, as well as a “braided” appearance reflecting linear combinations of the spin frequency with the average frame cadence.

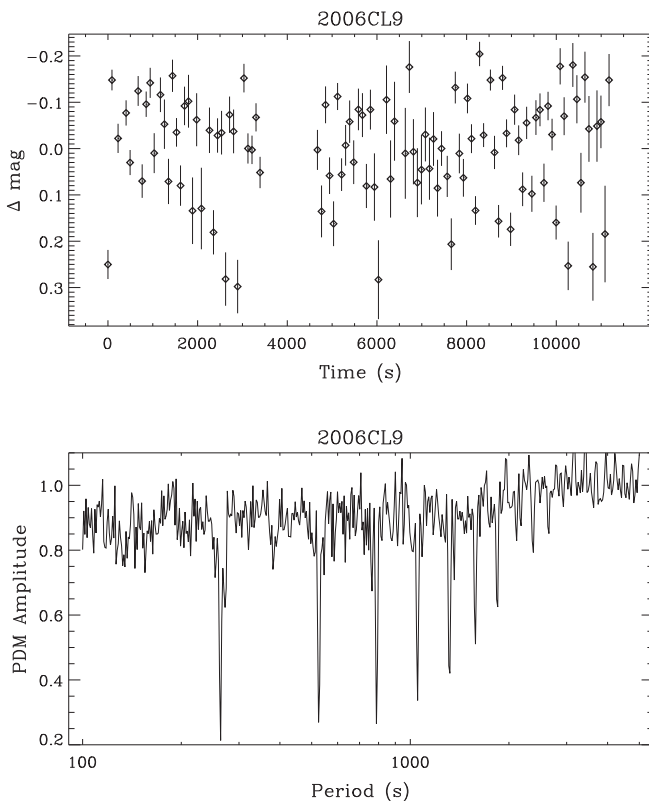


Fig. 2. (a) Top: Reduced and de-trended light curve of 2006 CL₉, illustrating the typical appearance of an FRA with a few-minute period. (b) Bottom: PDM spectrum for 2006 CL₉, showing lines at multiples of a 263.4 s period; the second multiple at 526.8 s corresponds to the rotation frequency.

2.3. Rotation period determination

We search for periodicities in the calibrated light curves using phase dispersion minimization (PDM; [Stellingwerf, 1978](#)). We have checked many of our results by using a periodogram analysis, but we see no cases in which the periodogram performs better than PDM. The PDM algorithm starts with a trial value of the period, folds the data to that period, and computes a χ^2 -like statistic by summing the error-weighted squares of the deviations of the data from a model. The value of the model at each data point is simply a low-order polynomial fit to the nearest N data points; thus PDM measures the tightness of the folded lightcurve about itself. We find that a linear fit with $N = 5$ produces good numerical stability and accuracy on simulated data. When the PDM statistic is plotted against trial period, periodicities appear as minima (“absorption lines”) in the PDM spectrum; [Fig. 2b](#) shows an example, for 2006 CL₉. We compute the statistical significance of a detected periodic signal by randomly scrambling the time ordering of the data set, recomputing the PDM spectrum, and checking for minima as low as or lower than the detected signal. Counting the fraction of times this happens in 200 Monte-Carlo scramblings gives an estimate of the probability P_{null} of the null hypothesis that the periodic signal is spurious. We quote the significance of the periodicity as $1 - P_{\text{null}}$.

2.4. Distribution of photometric residuals

For the 25 objects with measured or estimated periods, we construct smooth model light curves from Fourier fits to the data. The period is held fixed at the already determined value and the order of the fit is set at the value giving the first minimum in the reduced χ^2 . We then examine the distribution of residuals from these fits to measure our total photometric uncertainties.

The histogram in [Fig. 3](#) shows the distribution of residuals Δ_i for the 2742 photometric measurements of these 25 objects, scaled by the statistical errors σ_i^{stat} . If the measurement errors were normally distributed, if the statistical errors were perfectly estimated, and if the Fourier fits exactly represented the true underlying light curves (convolved with the 30 s exposure window), this histogram would be a Gaussian with unit standard deviation. We should expect a wider distribution both because of random effects not related to photon statistics (e.g. patchy time-variable transparency across the field) and because of actual structure in the true light curves not captured by the data or reflected in the smooth models.

The actual distribution of scaled residuals $\delta_i = \Delta_i / \sigma_i^{\text{stat}}$ is well fit by a Gauss–Hermite distribution with zero skewness,

$$f(\delta) = \frac{1}{4(3\pi)^{1/2}k} [1 + h_4(4\delta^4 - 12\delta^2 + 3)] \exp\left(-\frac{\delta^2}{2k}\right), \quad (1)$$

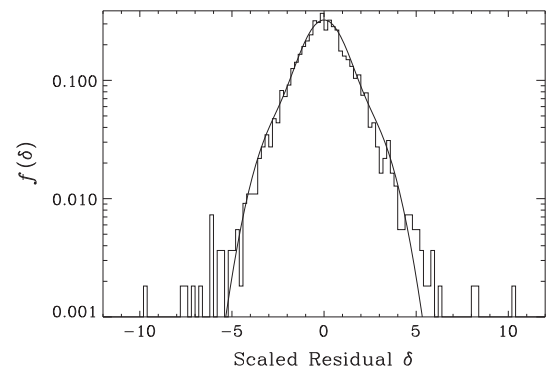


Fig. 3. Distribution of error-scaled residuals δ (histogram) for 2742 observations of 25 objects with measured or estimated periods and fitted model light curves. Smooth curve shows the adopted Gauss–Hermite distribution given by Eq. (1).

with $k = 1.29$ and $h_4 = 0.08$. This distribution, plotted as the smooth curve in Fig. 3, is consistent with the number of “outlier” points out to $\pm 6\sigma$. The small additional number of extreme outliers amounts to $<0.5\%$ of the data, or typically half a data point per observed object. We make no further attempt to model these extreme outliers since there is negligible chance they could have any tangible impact on the results. We assume that Eq. (1) describes the distribution of total photometric uncertainties for the entire data set.

2.5. Rotation period uncertainty

The statistical uncertainty in the period is determined by a Monte Carlo bootstrap. We simulate 50 light curves having the same period, and statistically the same shape, as the observed light curve, and compute the PDM spectrum; the variance in the period over the 50 trials is adopted as the error in the period. We obtain these simulated light curves from the Fourier fits, sampling at the observational cadence and adding non-Gaussian noise according to Eq. (1).

The fitted periods are subject to factor-of-2 ambiguities because one cannot know *a priori* whether to expect one or two (or more) brightness maxima per rotation period. As only two of our objects with clear periodicities were observed at phase angles $>50^\circ$, we assume that the period giving the double-peaked folded light curve is the correct one. There remains some ambiguity as to what constitutes a peak, particularly for the objects with lower amplitudes and signal-to-noise ratios. In this case we appeal to the Fourier fits, and call a local maximum above the mean brightness, bracketed by two local minima below the mean brightness, a peak. The results below represent our best efforts to resolve this ambiguity. Our principal results are not substantially changed if we are wrong by a factor of two on the possibly contentious cases.

A few slowly rotating objects, appearing to have unambiguous, double-peaked light curves, have been observed for only ~ 1 period or less. In those cases we provide an estimate of the period based purely on a visual inspection of the data.

2.6. Results

Of the 83 NEAs observed, 20 have periods that are measurable, mostly at $>99\%$ significance. Of these, 18 are FRAs with periods ranging from just under 2 h down to 102 s; only two are slow rotators with $P > 2$ h. Another 6 objects are slow rotators with periods estimated by eye to be ≥ 4 h. Two objects are candidates for fast, non-principal-axis (NPA) rotation for which one frequency is discernable in the PDM spectrum. We discuss each of these groups of objects in more detail below.

The majority (55 out of 83) of our observed NEAs have ambiguous light curves for which no measurements or estimates of rotation periods are possible. These light curves may be featureless, monotonically brightening or dimming, or may show non-repeating variations. This result contrasts with that of HW (and their publications referenced therein), who report 50 period measurements or estimates in a sample of 62 objects. We can attribute much of this difference to the greater fraction of larger objects ($H < 21$) in our sample and the low sensitivity of our observational strategy to slow rotation. Some of our ambiguous light curves are probably ambiguous merely because of larger photometric errors. The dashed and dotted lines in Fig. 1 show the error distribution for the ambiguous and unambiguous objects, respectively. The median error for the ambiguous objects is more than twice that for the unambiguous ones. But there is no evidence that we are unable to detect low-amplitude periodicities that HW can. Fig. 4 compares the joint distribution of periods and amplitudes (top) and the cumulative amplitude distribution (bottom) for the objects with

measured or estimated periods in the two samples; our sample actually contains more low-amplitude objects than HW's.

In the interest of brevity, we classify the ambiguous cases simply as non-detections of rotation, and will not discuss them individually in this paper. We return to the question of what these objects are in Section 5.

2.6.1. Fast periodic rotators

Eighteen objects have periods under 2 h that are detectable by PDM at significance of 80% or higher. These objects are listed in the upper section of Table 2, ordered by absolute magnitude, and their folded light curves are shown in Figs. 5a–5r. A few deserve specific comment.

2010 FC₈₁ was observed by Hicks et al. (2010) within two days of our observations. They report a period of 1174.80 ± 0.06 s, compared with our result of 1176.26 ± 0.83 s. Their data set consists of fewer data points (~ 70) than ours (~ 110), with comparable photometric errors, but acquired over two nights rather than one; this explains the extremely small formal error in their period. Their folded light curve indicates an amplitude of approximately 0.4 mag. This is slightly less than our 0.45 mag; however, their longer exposure time (200 s) may have produced some smearing.

2009 HM₈₂ was observed by Birtwhistle (2009) using a small telescope with very short (8–16 s) exposure times, over 2 nights, the second coinciding with our observations. He reports a period of 457.2 ± 0.4 s, which agrees with our result of 457.368 ± 0.096 s. His estimated amplitude of 0.9 mag is consistent with our value of 1.03 mag.

2006 CL₉ is also in the sample of HW, who observed it about two weeks after we did. They report a period of 522 ± 18 s and an amplitude of 0.39 mag, consistent with our values of 526.80 ± 0.45 s and 0.33 mag, respectively.

2007 DD was observed in the SALT survey of Kwiatkowski et al. (2010) about 12 days before our observations, and was found to have a complex light curve with a period of 267.44 ± 0.25 s and an amplitude of 0.8 mag. This agrees with our result of

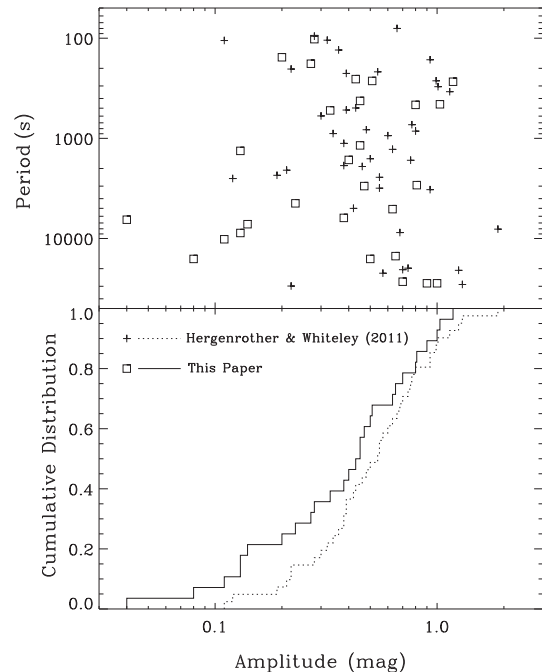
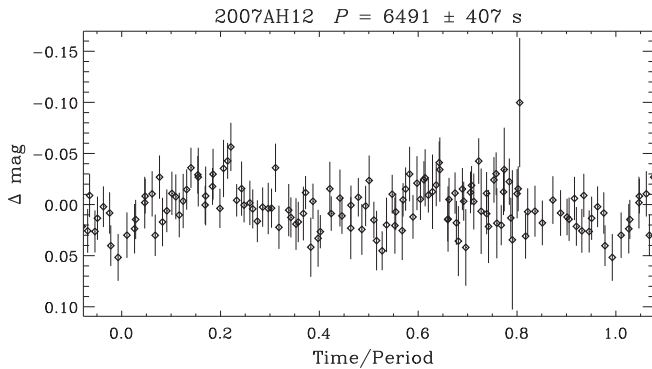
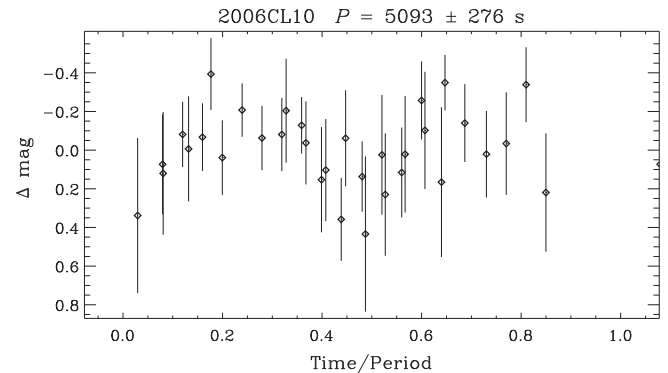
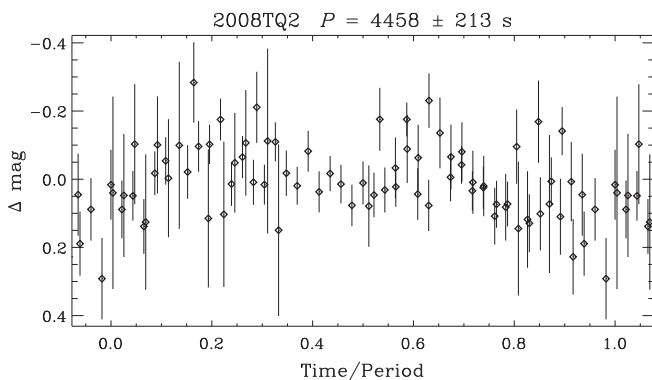
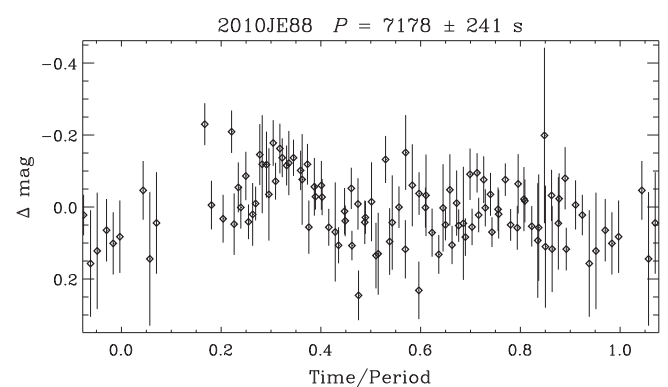


Fig. 4. Comparison of (top) the joint distribution of periods and amplitudes and (bottom) the cumulative distribution of amplitudes for objects with measured or estimated periods in this work (squares, solid line) and HW (crosses, dotted line). Error bars omitted for clarity.

Table 2Fast-rotating asteroids and fast-rotator candidates ($P < 2$ h).

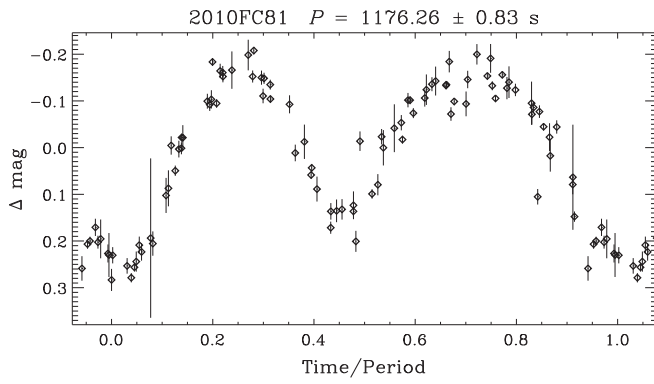
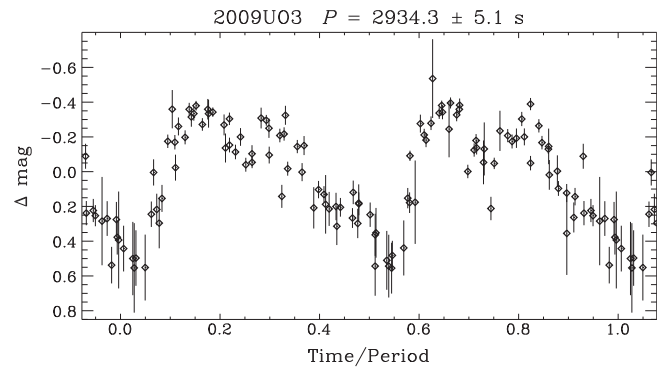
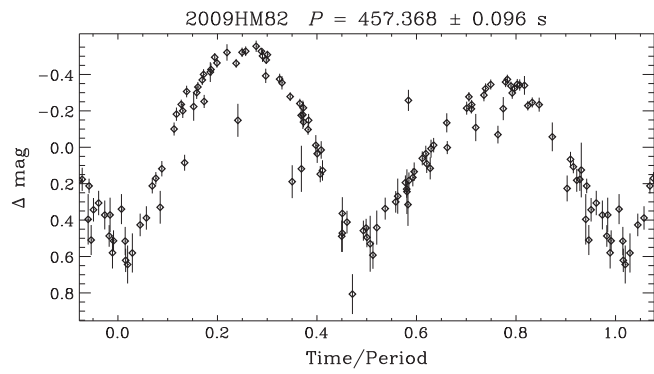
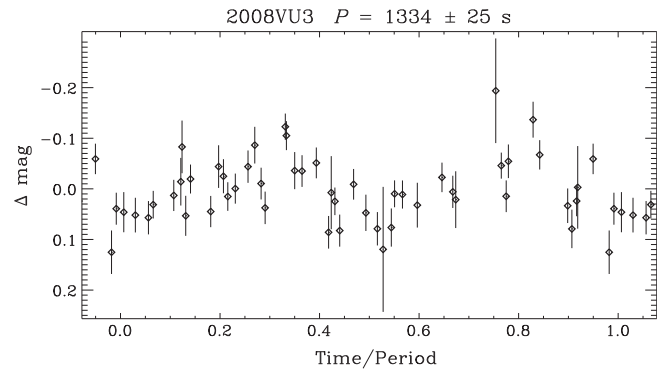
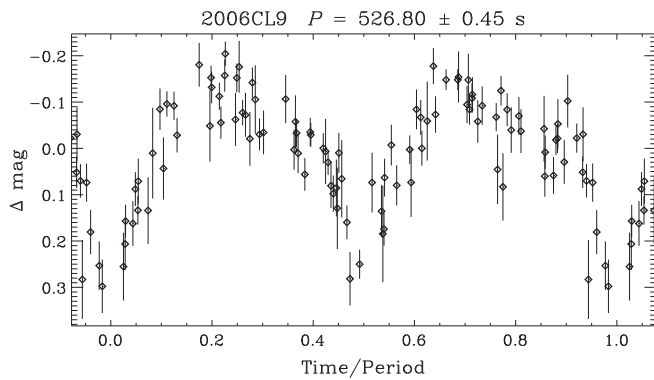
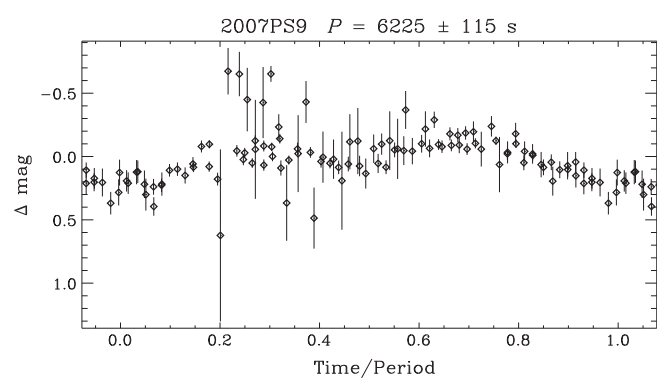
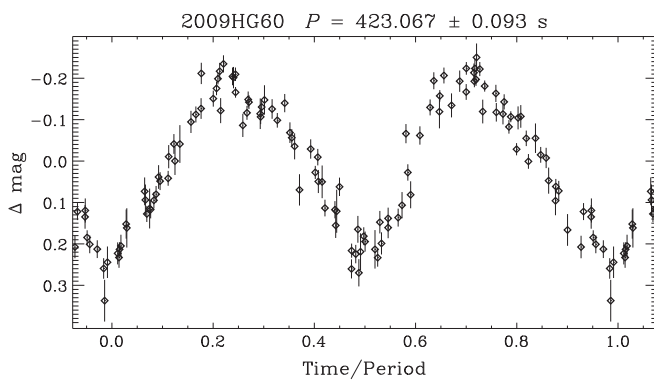
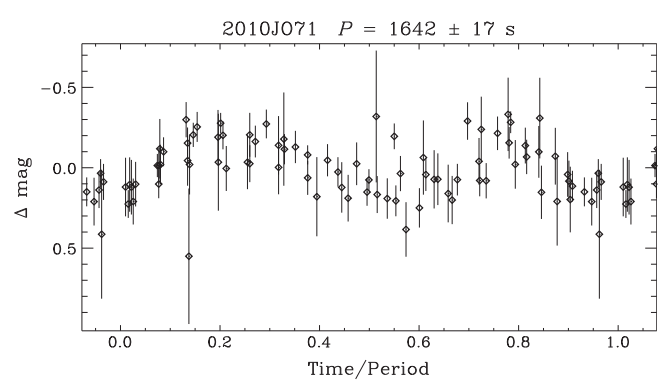
Name	H	P or $\frac{2\pi}{\omega}$ (s) ^a	\pm (s)	Significance ^b (%)	Trend ^c (mag s ⁻¹)	Amplitude ^d (mag)
<i>Periodic light curves (principal-axis rotators)</i>						
2007 AH ₁₂	20.5	6491	407	>99.5	-3.71×10^{-8}	0.04
2008 TQ ₂	20.9	4458	213	89.0	-1.79×10^{-6}	0.23
2006 CL ₁₀	21.1	5093	276	84.5	2.25×10^{-5}	0.63
2010 JE ₈₈	21.5	7199	241	>99.5	-1.27×10^{-5}	0.14
2010 FC ₈₁	21.9	1176.26	0.83	>99.5	-2.43×10^{-5}	0.45
2009 HM ₈₂	22.5	457.368	0.096	>99.5	2.09×10^{-6}	1.03
2006 CL ₉	22.7	526.80	0.45	>99.5	3.01×10^{-6}	0.33
2009 HG ₆₀	22.7	423.067	0.093	>99.5	-9.54×10^{-6}	0.45
2009 UO ₃	23.0	2934.3	5.1	>99.5	1.56×10^{-5}	0.81
2008 VU ₃	23.3	1334	25	99.0	-8.35×10^{-6}	0.13
2007 PS ₉	23.5	6225	115	>99.5	-1.84×10^{-5}	0.38
2010 JO ₇₁	23.9	1641.8	17	>99.5	-2.32×10^{-5}	0.40
2008 CP	24.0	2997.1	7.6	>99.5	4.46×10^{-5}	0.47
2008 UT ₅	24.5	256.43	0.39	>99.5	3.15×10^{-5}	0.43
2008 CC ₇₁	24.9	272.2	5.0	80.0	-1.27×10^{-5}	1.18
2010 KK ₃₇	25.7	102.3313	0.0092	>99.5	-4.79×10^{-6}	0.28
2007 DD	25.8	267.257	0.11	>99.5	5.72×10^{-8}	0.51
2009 HK ₇₃	26.3	179.960	0.023	>99.5	-1.50×10^{-7}	0.27
<i>Candidate quasiperiodic light curves (non-principal-axis rotators)</i>						
2007 EV	25.0	463.45	0.55	85.0	3.27×10^{-5}	0.8
2010 TM ₃	20.5	155.09	0.13	64.0	4.63×10^{-5}	0.2

^a Period, for principal-axis rotators, or 2π divided by the strongest detectable frequency for non-principal-axis candidates.^b $1 - P_{\text{null}}$, where P_{null} is the probability of the null hypothesis that the periodic signal is spurious.^c Linear trend removed from the light curve; correction for residual flat fielding/illumination errors.^d Full max-to-min amplitude.**Fig. 5a.** Folded light curve for 2007 AH₁₂.**Fig. 5c.** Folded light curve for 2006 CL₁₀.**Fig. 5b.** Folded light curve for 2008 TQ₂.**Fig. 5d.** Folded light curve for 2010 JE₈₈.

267.257 ± 0.11 s for the period, though our light curve (Fig. 5q), while similarly complex, shows a smaller amplitude of 0.51 mag.

2009 UO₃ is listed in the NASA/JPL Solar System Dynamics web-site with a period of approximately 1500 s reported by E. Ryan in

an Email sent about 2 weeks before our observations. This period is approximately half our value of 2934.3 ± 5.1 s. Our light curve (Fig. 5i) shows two clear maxima and minima per cycle at the longer period, which we prefer for this reason.

Fig. 5e. Folded light curve for 2010 FC₈₁.Fig. 5i. Folded light curve for 2009 UO₃.Fig. 5f. Folded light curve for 2009 HM₈₂.Fig. 5j. Folded light curve for 2008 VU₃.Fig. 5g. Folded light curve for 2006 CL₉.Fig. 5k. Folded light curve for 2007 PS₉.Fig. 5h. Folded light curve for 2009 HG₆₀.Fig. 5l. Folded light curve for 2010 JO₇₁.

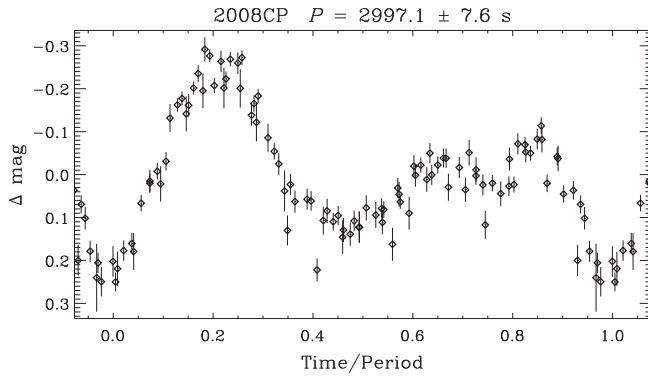


Fig. 5m. Folded light curve for 2008 CP.

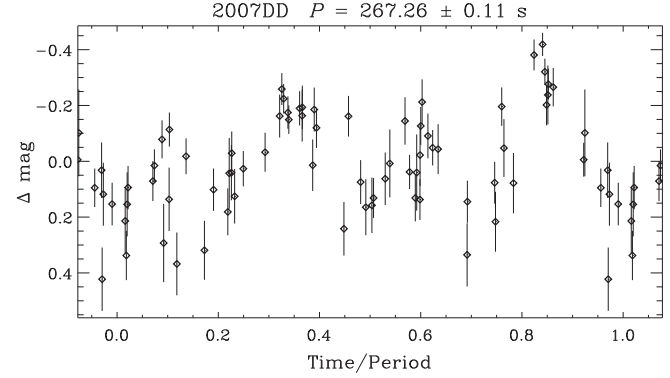
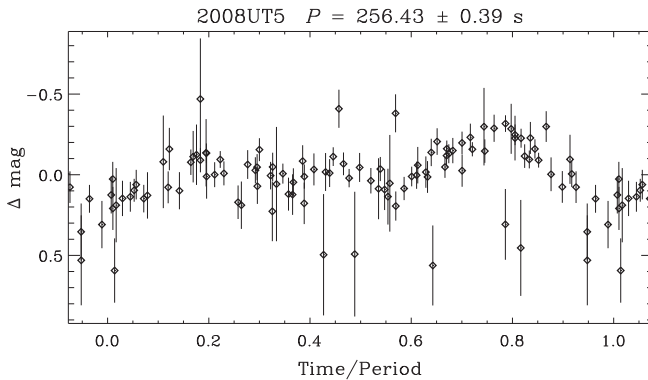
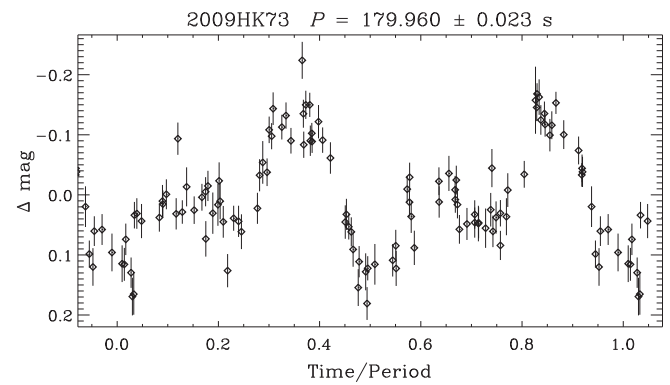
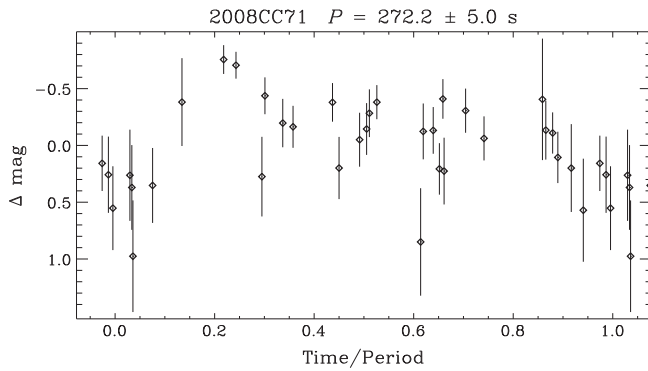
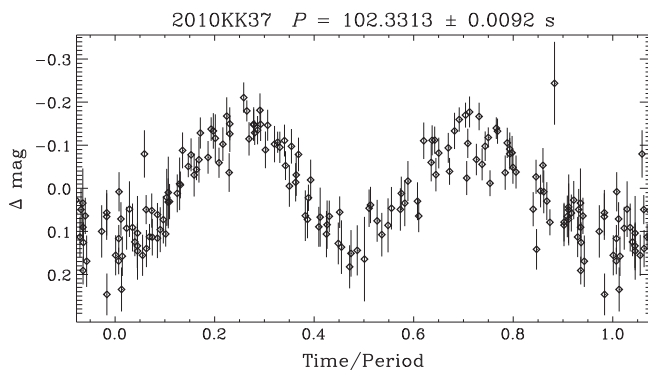


Fig. 5q. Folded light curve for 2007 DD.

Fig. 5n. Folded light curve for 2008 UT₅.Fig. 5r. Folded light curve for 2009 HK₇₃.Fig. 5o. Folded light curve for 2008 CC₇₁.Fig. 5p. Folded light curve for 2010 KK₃₇.

2.6.2. Fast quasi-periodic rotators

Two objects show the same “hallmarks” of fast rotation seen in Fig. 2a, but have no detectable periodicities. These objects are listed in the lower section of Table 2. The case with the largest amplitude is 2007 EV. Fig. 6a shows the full calibrated and detrended light curve; clearly there is frame-to-frame variability much larger than the photometric errors, and the vaguely braided appearance is very reminiscent of Fig. 2a. However, the PDM spectrum (Fig. 6b) shows only a few weak lines at multiples of 231.73 s, at a significance of 85%. Folding the data to the second multiple (i.e., assuming a double-peaked light curve at the correct period) gives the result in Fig. 6c, with residuals still much larger than the errors. We conclude that this is not a simply periodic rotator. Unfortunately, obtaining a quasiperiodic fit to a tumbling body requires a long period of observation (Pravec et al., 2005), and our data set is evidently not long enough. We have attempted, without success, to identify additional frequencies using both the periodogram and “windowclean” (Mueller, private communication) methods. Our conclusion is that conclusively identifying non-principal-axis rotation requires a substantially different observational strategy than we have employed here, and that our present strategy can identify only likely NPA candidates.

Fig. 7 shows the light curve for the other NPA candidate, 2010 TM₃. PDM identifies a periodicity at 155.09 s at low (64%) significance. We admit to being somewhat suspicious of the low (0.2 mag) amplitude, as only 2 out of 18 of our periodic fast rotators have amplitudes this small. On the other hand, it is >6 times larger than the mean photometric error for this object, including the correction from Eq. (1). Rapid NPA rotation in an object this large ($H = 20.5$) would be unusual, so this object should be re-observed at a future opportunity.

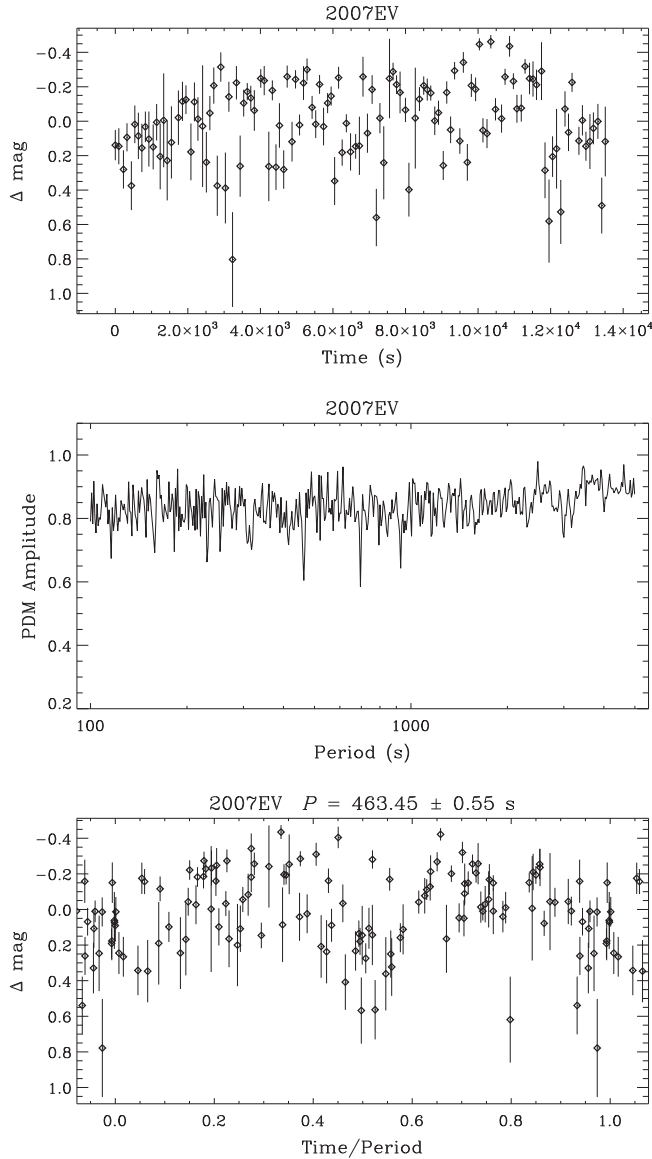


Fig. 6. (a) Top: De-trended light curve of 2007 EV; rapid frame-to-frame variability and “braided” appearance strongly suggest fast rotation. (b) middle: PDM spectrum for 2007 EV, showing lines at 1, 2, 3, and 4 times a single-peak period of 231.73 s. (c) Bottom: Light curve for 2007 EV folded to a period of 463.45 s; large residuals suggest a quasiperiodic, rather than simply periodic, solution.

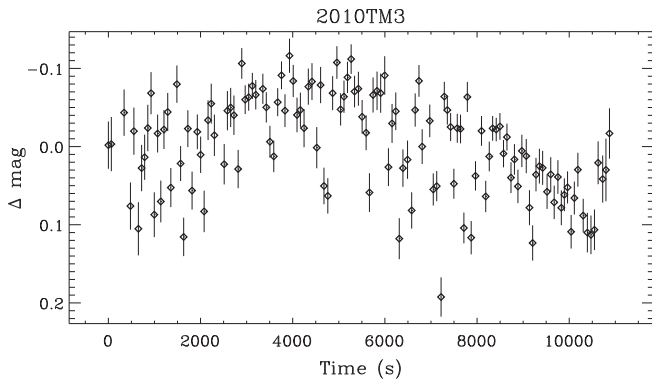


Fig. 7. De-trended light curve for the non-principal-axis candidate 2010 TM₃.

In our statistical analysis of the FRA fraction below, neither of the NPA candidates is counted as a detection of fast rotation.

2.6.3. Slow rotators

Eight objects have rotation periods >2 h that can be measured or estimated; these are listed in Table 3.

2006 BN₅₅ and 2010 TC₅₅ have periods measured by PDM to be $10,180 \pm 160$ s and 8807 ± 101 s, respectively, at $>99.5\%$ significance. Their folded light curves are shown in Figs. 8a and 8b and details are given in the top section of Table 3.

Six objects have light curves strongly suggesting that they were observed for between $1/4$ and 1 period. These are shown in Figs. 9a–9f. We have estimated periods from visual extrapolation of the light curves. The results are listed in the second and third sections of Table 3. 2008 SE was observed by Warner (2009) 12 days before we did; he obtains a period of $16,450 \pm 180$ s and an amplitude of 0.7 mag, reasonably consistent with our estimates of 16,000 s and 0.5 mag, respectively.

3. Sensitivity, incompleteness, and debiasing

The simple raw counts of detected periodic rotators and their distribution in parameter space cannot by themselves reveal the true spin state distribution. Detections do not constitute a census of the population because for any photometric error, and any object, there are geometries in which a periodicity, even if present, will not be detected. In order to translate the raw counts of FRAs into actual constraints on the FRA fraction and spin rate distribution, it is essential to understand our FRA detection sensitivity and de-bias the results accordingly.

Estimating the fraction of the time that we fail to detect periodicities actually present in the data requires some *a priori* model for the properties of the intrinsic light curves we are trying to observe. We construct a large library of simulated light curves using our thermophysical code TACO¹ (Statler, 2009). TACO uses a standard triangular-tile representation of the surface; the models used here contain 3184 tiles. Shadowing is handled explicitly. The tiles have a rough-surface bidirectional reflectance computed using Hapke’s formalism (Hapke, 1981, 1984, 1986, 2002; Hapke and Wells, 1981). We adopt the Hapke parameters for average S-class asteroids obtained by Helfenstein and Veverka (1989): a single-scattering albedo of $w = 0.23$, a surface roughness or mean slope angle of $\bar{\theta} = 20^\circ$, and an asymmetry factor of $\xi = -0.35$. We do not include the opposition effect, since most of our sample is observed at moderate phase angle, and the change in phase angle during the observation is negligible. These parameters are assumed to be constant over the entire surface. We generate asteroid shapes using the “Gaussian random sphere” formalism of Muinonen and Lagerros (1998), as described in Section 2.2 of Statler (2009). These objects are statistically consistent with the distribution of shapes obtained from light curves of well-studied objects. We create 40 such objects, and for each object calculate light curves for 400 rotation pole positions uniformly distributed over the sphere and 10 phase angles from 0° to 90° at 10° increments. This gives us a library of 160,000 light curves representative of the typical photometric variability of the NEA population.

We use the simulated light curves to assess our observational sensitivity to different rotation periods. The approach described here is a general method that, with a sufficiently large data set free of selection biases, could be used to obtain the de-biased NEA period distribution as a function of absolute magnitude. In this paper we limit the application to a simpler question: *what is the fraction F of objects that are fast rotators, as a function of H ?*

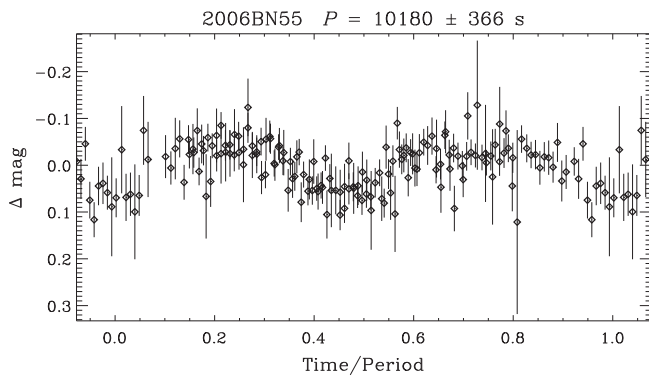
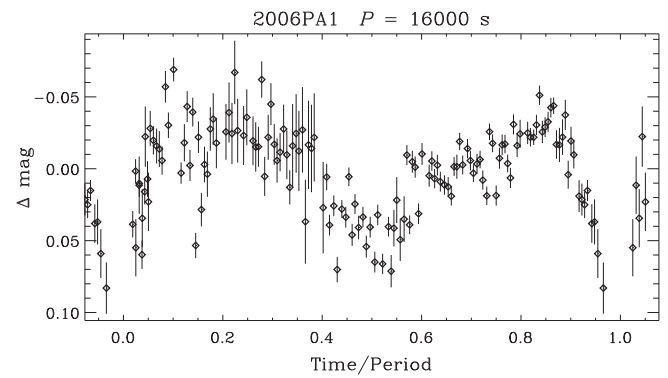
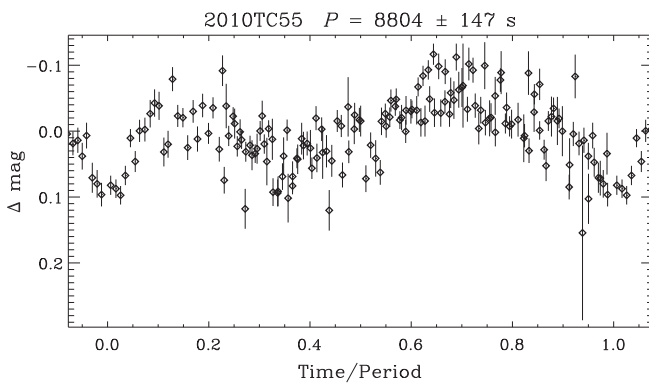
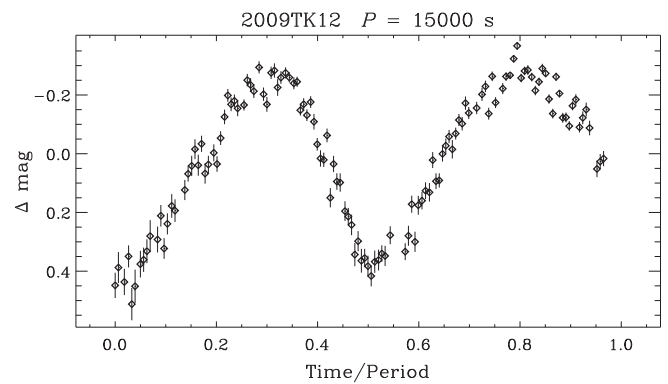
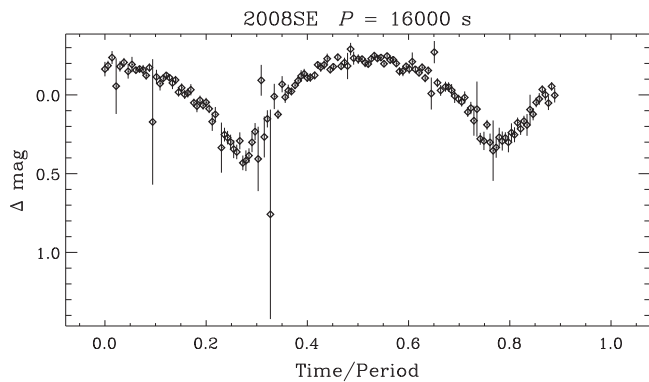
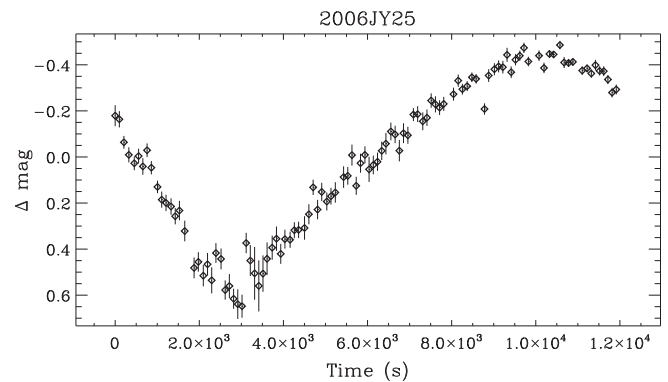
Our Monte Carlo code SALSA² implements this approach as follows. We first collect the actual light curves for all N_{obs} observed

¹ Thermophysical Asteroid Code, Obviously; the thermophysical aspects (e.g., heat conduction and radiation recoil) are not used in this application.

² Simulated Asteroid Lightcurve Sensitivity Assessment.

Table 3Slow-rotating asteroids ($P > 2$ h).

Name	H	P (s)	\pm (s)	Significance	Trend (mag s^{-1})	Amplitude (mag)
<i>Periodic light curves (principal-axis rotators)</i>						
2006 BN ₅₅	19.8	10,180	366	>99.5%	2.27×10^{-6}	0.11
2010 TC ₅₅	20.2	8804	147	>99.5%	-8.31×10^{-7}	0.13
<i>Partial light curves (period estimates possible)</i>						
>1/2 Period observed						
2008 SE	19.4	16,000	—	—	—	0.50
2006 PA ₁	19.7	16,000	—	—	—	0.08
2009 TK ₁₂	20.6	15,000	—	—	—	0.65
<1/2 but >1/4 period observed						
2006 JY ₂₅	20.4	28,000	—	—	—	1.0
2006 VC	19.9	28,000	—	—	—	0.9
2008 VH ₁₄	23.6	27,000	—	—	—	0.7

**Fig. 8a.** Folded light curve for 2006 BN₅₅.**Fig. 9b.** Light curve for 2006 PA₁.**Fig. 8b.** Folded light curve for 2010 TC₅₅.**Fig. 9c.** Light curve for 2009 TK₁₂.**Fig. 9a.** Light curve for 2008 SE.**Fig. 9d.** Light curve for 2006 JY₂₅.

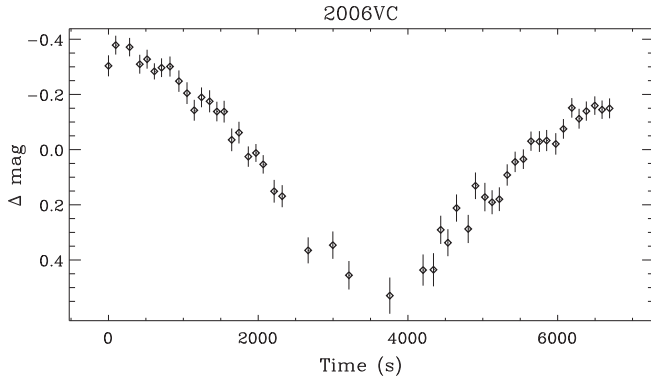


Fig. 9e. Light curve for 2006 VC.

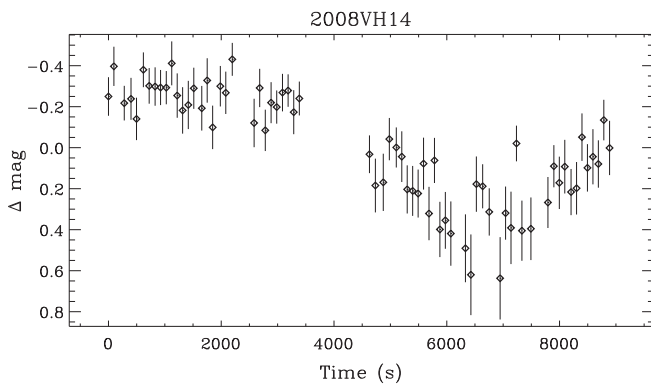


Fig. 9f. Light curve for 2008 VH₁₄.

objects in a particular absolute magnitude bin (regardless of whether they have measurable periods), the mean phase angles of the observations, and the number N_d of detected fast rotators, where we define a “detection” to be a periodic signal at $\geq 99\%$ confidence. A SALSA trial starts by picking a test value of the true FRA fraction F ; the goal is to calculate the probability that this value of F would result in N_d detections in a sample of N_{obs} objects. We imagine a trial sample of N_{obs} objects, each of which has a probability F of being an FRA, and create a Monte-Carlo realization of that sample. Suppose that realization contains N_F FRAs. If $N_F < N_d$, the trial is counted as a failure, since there is no way it could result in N_d detections.³ If $N_F \geq N_d$, we simulate observed light curves for N_F objects as follows. We randomly pick N_F objects and orientations, without repetition, from the library of simulated objects, which we link with N_F actual light curves and corresponding phase angles randomly chosen from the N_{obs} observed objects. For each simulated object, we pick the light curve from the library most closely matching the phase angle of the linked observation. We randomly assign a rotation period between 1 min (the extreme lower limit of what we could hope to detect with 30 s exposures) and 2 h. In this step we have to make an assumption for the prior distribution of periods within this FRA range. We adopt a distribution that is flat in $\log P$ between the limits, which is broadly consistent with the accumulated data (Warner et al., 2009).⁴ We then sample the light curve at the actual exposure time (integrating over the exposure) and frame spacing of the linked

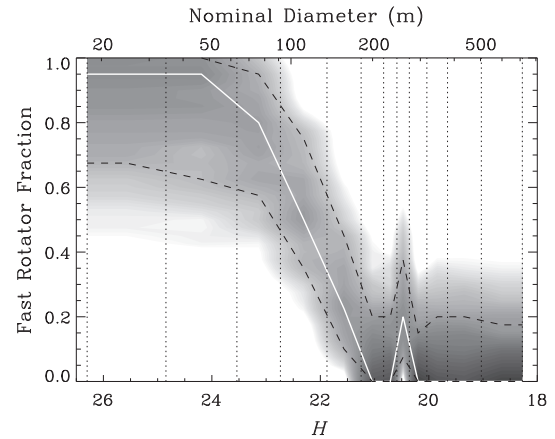


Fig. 10. The de-biased (completeness-corrected) fast-rotator fraction F is plotted against absolute magnitude H (lower scale) and nominal diameter (upper scale, assuming spherical objects with albedo of 0.17). Vertical dotted lines indicate boundaries of bins containing nearly equal numbers of observed objects. Grayscale indicates probability density $P(F)$ in each absolute magnitude bin. Solid line connects the most probable value of F in each bin; dashed lines enclose 68% of the integrated probability, corresponding to a 1σ error region. Note the abrupt transition, spanning less than a factor of 3 in diameter, between the small objects, the strong majority of which are fast rotators, and the larger objects, almost none of which are fast rotators.

observation, and add noise according to Eq. (1). Finally, we send the light curve through the same PDM analysis described above to determine whether a periodicity is detected at $\geq 99\%$ significance. We do this for each of the N_F FRAs in the trial sample, and count the number of detections. If this number matches N_d , the trial is a success; otherwise it is a failure. We repeat this procedure for 300 trials at the same assumed value of F , and the fraction of successful trials is then our estimate of the likelihood that this value would produce the observed number of FRAs. We then move to the next value of F , mapping out the entire likelihood function. Adopting a flat prior for F , the normalized likelihood then gives us the Bayesian posterior probability density $P(F)$ for the fast-rotator fraction.

4. The fast-rotator fraction

Fig. 10 shows the de-biased FRA fraction F as a function of absolute magnitude H . Nominal diameters for spherical bodies with an albedo of 0.17 are indicated along the top of the figure. The probability density $P(F)$ is shown in grayscale, for 12 bins in absolute magnitude containing nearly equal numbers of observed objects. The solid line connects the most probable values of F in every bin. The dashed lines enclose 68% of the integrated probability, corresponding to a 1σ error region. Several striking aspects of this figure are evident:

- *Essentially nothing larger than $H = 21.4$ ($D = 170$ m) is a fast rotator.* The most probable FRA fraction in all bins with $H \leq 21.4$ but one is zero. The small spike at $H = 20.5$ corresponds to the single object 2007 AH₁₂ (Fig. 5a), with a 1.8 h period.⁵
- *Nearly everything smaller than $H = 23.6$ ($D = 60$ m) is a fast rotator.* The FRA fraction for $H \geq 23.6$ is consistent with unity at the 1σ level.
- *The transition happens over less than a factor of 3 in size (a span of 2.2 magnitudes in H).*

³ We consider the probability of false detections, at a 99% confidence threshold, to be negligibly small.

⁴ Repeating the calculation using a distribution that is flat in P yields nearly identical results.

⁵ An anonymous referee points out that the factor-of-two ambiguity could permit 2007 AH₁₂ to be a slow rotator with a quadruple-peaked light curve. 2008 TQ₂ and 2006 CL₁₀, listed as FRA candidates in Table 2, have significances $< 99\%$ and are therefore not counted as detections.

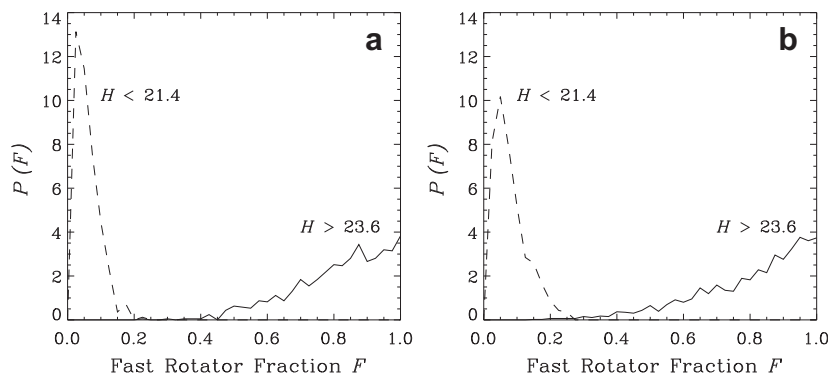


Fig. 11. Probability densities $P(F)$ for the fast-rotator fraction F among (solid lines) small objects ($H > 23.6$, two leftmost bins in Fig. 10) and (dashed lines) large objects ($H < 21.4$, six rightmost bins in Fig. 10). (a) Results using the full sample. (b) Results using only objects with mean photometric errors (Table 1) better than the median value.

The difference between the large and small populations is highlighted in Fig. 11a. The dashed line shows $P(F)$ computed for all objects with $H < 21.4$; the solid line shows the same function for all objects with $H > 23.6$. At 95% confidence, no more than 13% of NEAs with $18.5 < H < 21.4$ are FRAs, and no less than 56% of NEAs with $23.6 < H < 26.3$ are FRAs. The rather generous lower limit on F for the smallest objects is merely a result of small number statistics, and this constraint would tighten with a significantly larger sample.

To demonstrate that this result is not biased by—and is in fact improved by—using all of the data, even those with larger photometric errors, we show in Fig. 11b the same probability densities computed using only the objects with $\langle \sigma_{\text{phot}}^{\text{stat}} \rangle$ less than (i.e., better than) the median. The results are completely consistent with those from the full sample. The only difference is that F is less well constrained by less data: here the 95% confidence limits are $F < 18\%$ for the large objects and $F > 49\%$ for the small objects.

HW also report a steep rise in the FRA fraction among smaller objects, based on their raw counts of detected periodicities uncorrected for incompleteness and without confidence limits. Their estimated fractions, $F \geq 0.68$ for $20 < H < 27.4$, $F \geq 0.60$ for $22 \leq H < 27.4$, and $F \geq 0.79$ for $24 \leq H < 27.4$, are broadly consistent with our results, but suggest an even steeper rise in the FRA fraction faintward of $H = 21$.

5. Interpretation and discussion

Models of ensemble evolution through the YORP cycle (e.g. Rossi et al., 2009) tend toward flat distributions in spin frequency, between zero (nonrotating) and a maximum, presumably determined either by the peak of the natural YORP cycle or the strength limit of the material. Let us assume that this were the case: that at every H the distribution were a “top-hat” distribution in frequency: flat between 0 and a sharp upper cutoff at $2\pi/P_{\text{min}}(H)$. The fraction of objects with periods under 2 h would be

$$F(H) = 1 - \frac{P_{\text{min}}(H)}{2 \text{ h}}. \quad (2)$$

From the most probable $F(H)$ determined above (Fig. 10), we calculate the implied spin limit. We find that close to half of our objects with measured periods spin faster than this putative $P_{\text{min}}(H)$, which drops from 2 h (7200 s) at $H = 21.0$ to 0.5 h (1800 s) at $H = 23.0$. Thus the actual spin distribution extends to higher frequencies than the top-hat distribution with the same fraction of FRAs.

The actual distribution is a superposition of all of the evolutionary paths of the population, and its detailed shape can constrain models of that evolution, as we see in the simple examples above.

In this paper we have used our SALSA approach only to obtain the fraction of NEAs (per H bin) with periods $P < 2$ h. There is nothing—other than sample size—preventing us from using the same approach to determine the fraction of objects with $P < 1$ h, with $P < 0.5$ h, and so on, thereby building up the cumulative period distribution as a function of absolute magnitude. Combining our sample with others that are free from reporting bias and that have comparably well determined photometric errors is the only sure route to that desired result. Thus, systematic, rather than piecemeal, publication of light curve data is essential.

Objects with ambiguous light curves make up over half of our sample and about 15% of the HW sample. Some of this difference in the ambiguous fraction can be attributed to differences in sensitivity and signal-to-noise ratio; HW observed nearly half of their objects at $V < 18$, whereas fewer than 20% of our objects were this bright when observed. However, as we showed in Fig. 4, we actually detect more low-amplitude periodicities than do HW, and our single brightest object at the epoch of observation, 2006 UQ₁₇, has an ambiguous light curve. We see a steeply declining fraction of ambiguous objects toward fainter absolute magnitudes: 80% for objects brighter than $H = 20$, but only 37% for objects fainter than $H = 23$. One expects a certain inevitable fraction of ambiguous objects simply because of unfavorable geometry (e.g., pole-on orientation), but this would not explain the trend with H . The decline has to reflect an intrinsic trend in the population. There are three possibilities: (1) The ambiguous objects are very slow rotators. The known presence of slow rotators for diameters above 200 m is consistent with this alternative. (2) The ambiguous objects are super-fast rotators, with periods under 1 min, to which we have no sensitivity. Currently 6 objects are known with periods < 100 s (Warner et al., 2009), but all but one are fainter than $H = 23$. These objects could be present but would not account for the trend since they are all small. And finally, (3) the ambiguous objects could be nearly axisymmetric objects with intrinsically very low amplitude light curves.

Our debiasing procedure does rely, to some extent, on the assumption that the simulated objects created by the Gaussian random sphere formalism are representative of the population of FRAs. The correlation coefficients describing the shape statistics were derived by Muinonen and Lagerros (1998) from shape fits to well-studied objects. It is possible that the sample of objects available in 1998 was biased toward higher amplitude light curves, and therefore less axisymmetric shapes. We have tested the sensitivity of our results to this possibility by re-running the SALSA analysis with the light curve amplitudes of half of our simulated objects decreased by a factor of 2. The results, shown in Fig. 12, are consistent with the results from the unaltered library to within 1σ in all bins but one. The very modest effect is to make the tran-

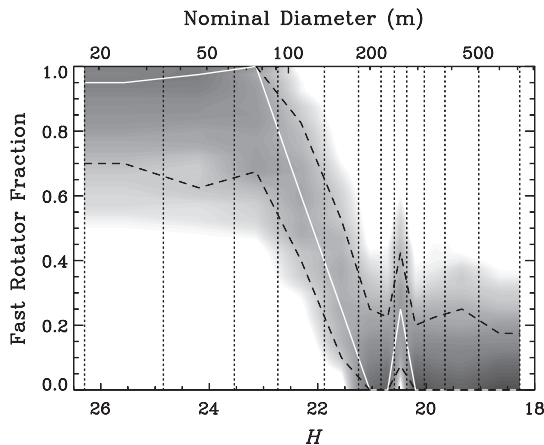


Fig. 12. Assessing the effect of possible bias in the simulated object library toward more elongated shapes: same as Fig. 10, but with the amplitudes of half of the library light curves reduced by a factor of 2.

sition from $F \approx 0$ to $F \approx 1$ even more abrupt. Thus our conclusions are not affected by moderate bias in the shapes of the simulated objects.

In principle, a population of nearly axisymmetric FRAs, with near-zero amplitudes, could be “hiding.” But if that were the case, our results for the FRA fraction F would represent lower limits. The fact that F is already close to unity for the small objects strongly suggests that there is not a large hidden population of small axisymmetric objects. Axisymmetric fast rotators could be hiding preferentially among the larger objects for which we obtain $F \approx 0$, which could account for the trend in the ambiguous fraction. There is no particular reason to expect the shape distribution to change rapidly with size in this region. But neither is there any reason to expect the spin distribution to change rapidly with size—and yet it clearly does.

6. Summary and conclusions

We have described optical light curve observations of a sample of 83 sub-kilometer-sized near-Earth asteroids. Approximately one third of those observations yield measurements or estimates of rotation period, most of which are in the fast-rotating regime with periods under 2 h. We have introduced a fully general Monte Carlo procedure for de-biasing the observed period distribution, and used that procedure with the present modest sample to constrain the fraction of NEAs that are fast rotators as a function of absolute magnitude. We find that the FRA fraction rises sharply from zero to a value statistically consistent with unity over a span of only 2.2 magnitudes from $H = 21.4$ to $H = 23.6$, corresponding to a factor 2.8 in size. Almost nothing larger than 170 m, and almost everything smaller than 60 m, is a fast rotator. We also show that the spin distribution extends to faster rotation than would be predicted by a top-hat distribution in frequency having the same FRA fraction.

Improving knowledge of the spin rate distribution to the level where it will become an effective constraint on the physical properties of NEAs and on their dynamical evolution will require larger samples, and homogeneous, unbiased reporting of the data. It is absolutely essential that the photometric data, with accurate errors, be made available for *all* objects observed, not only those that yield period measurements; the details of non-detections are as important as those of the detections for debiasing the results. In addition, observing strategies should be expanded to probe the more difficult parts of parameter space and determine the nature

of the objects with ambiguous light curves. The contribution of very slow rotators can be determined using modest aperture telescopes. The NEOWISE mission observed several dozen sub-km-sized NEAs with a ~ 3 h cadence (Mainzer et al., 2011a); these data will be a significant contribution when fully analyzed. Ground-based efforts will require dedicated multi-night observations of individual objects. Coordinated observations from multiple ground-based stations would be helpful. Finding the contributions from extremely fast rotators and from nearly axisymmetric objects will require short exposures and high photometric accuracy, respectively, both of which imply a need for large aperture.

Acknowledgments

The authors are grateful to many people for helpful comments and suggestions during the course of this work, including Derek Richardson, Steve Chesley, Dan Scheeres, Beatrice Mueller, Al Harris, Don Terndrup, Bill Bottke, Larry Molnar, David Polishook, Peter Pravec, Nalin Samarasinha, David Vokrouhlický, and Mangala Sharma. The assistance of the staff at MDM Observatory is gratefully acknowledged, as is the observing assistance of Ohio University undergraduate students Jess Wilhelm, Tomomi Watanabe, Kyle Uckert, and Keith Hawkins. TSS was supported in part by the Independent Research and Development program while on detail to NSF under the Intergovernmental Personnel Act. The results and opinions expressed in this paper are those of the authors and do not reflect the views of the National Science Foundation. DCF was supported by a NASA Harriet G. Jenkins Predoctoral Fellowship and a NASA Ohio Space Grant Consortium Doctoral Fellowship. KMS received support from a NASA Ohio Space Grant Consortium Senior Scholarship. We thank the creators and maintainers of the NEODYs, NEO Confirmation List, Spaceguard Priority List, and JPL Small-Body Database websites. This work has made use of NASA's Astrophysics Data System Bibliographic Services.

References

- Birtwhistle, P., 2009. Lightcurves for five close approach asteroids. *Minor Planet Bull.* 36 (October), 186–187.
- Bottke Jr., W.F., Vokrouhlický, D., Rubincam, D.P., Nesvorný, D., 2006. The Yarkovsky and Yorp effects: Implications for asteroid dynamics. *Annu. Rev. Earth Planet. Sci.* 34 (May), 157–191.
- Chesley, S.R., Vokrouhlický, D., Bottke, W.F., 2008. Distribution of NEA spin axis obliquities from measured thermal accelerations. *Bull. Am. Astron. Soc.* 40, 435.
- Hapke, B., 1981. Bidirectional reflectance spectroscopy. I – Theory. *J. Geophys. Res.* 86 (April), 3039–3054.
- Hapke, B., 1984. Bidirectional reflectance spectroscopy. III – Correction for macroscopic roughness. *Icarus* 59 (July), 41–59.
- Hapke, B., 1986. Bidirectional reflectance spectroscopy. IV – The extinction coefficient and the opposition effect. *Icarus* 67 (August), 264–280.
- Hapke, B., 2002. Bidirectional reflectance spectroscopy 5. The coherent backscatter opposition effect and anisotropic scattering. *Icarus* 157 (June), 523–534.
- Hapke, B., Wells, E., 1981. Bidirectional reflectance spectroscopy. II – Experiments and observations. *J. Geophys. Res.* 86 (April), 3055–3060.
- Harris, A.W., 1996. The rotation rates of very small asteroids: Evidence for ‘Rubble Pile’ structure. *Lunar Planet. Sci.* 27, 493–494 (abstracts).
- Helfenstein, P., Veveřka, J., 1989. Physical characterization of asteroid surfaces from photometric analysis. In: Binzel, R.P., Gehrels, T., Matthews, M.S. (Eds.), *Asteroids II*. pp. 557–593.
- Hergenrother, C.W., Whiteley, R.J., 2011. A survey of small fast rotating asteroids among the near-Earth asteroid population. *Icarus* 214 (July), 194–209.
- Hicks, M., Mayes, D., Somers, J., 2010. Broadband photometry of the potentially hazardous asteroid 2010 FC81. *Astronomer's Telegram* 2647 (May), 1.
- Holsapple, K.A., 2005. Asteroid spin data: No Evidence of rubble-pile structures. In: Mackwell, S., Stansbery, E. (Eds.), 36th Annual Lunar and Planetary Science Conference, Lunar and Planetary Institute Science Conference Abstracts, vol. 36, pp. 2329–+.
- Holsapple, K.A., 2007. Spin limits of Solar System bodies: From the small fast-rotators to 2003 EL61. *Icarus* 187 (April), 500–509.
- Kwiatkowski, T. et al., 2010. Photometric survey of the very small near-Earth asteroids with the SALT telescope. I. Lightcurves and periods for 14 objects. *Astron. Astrophys.* 509 (January), A94.
- Mainzer, A. et al., 2011a. NEOWISE observations of near-Earth objects: Preliminary results. *Astrophys. J.* 743 (December), 156.

- Mainzer, A. et al., 2011b. NEOWISE studies of spectrophotometrically classified asteroids: Preliminary results. *Astrophys. J.* 741 (November), 90.
- Muironen, K., Lagerros, J.S.V., 1998. Inversion of shape statistics for small Solar System bodies. *Astron. Astrophys.* 333 (May), 753–761.
- Pravec, P., Harris, A.W., Scheirich, P., Kušnirák, P., Šarounová, L., Hergenrother, C.W., Mottola, S., Hicks, M.D., Masi, G., Krugly, Y.N., Shevchenko, V.G., Nolan, M.C., Howell, E.S., Kaasalainen, M., Galád, A., Brown, P., Degraff, D.R., Lambert, J.V., Cooney, W.R., Foglia, S., 2005. Tumbling asteroids. *Icarus* 173 (January), 108–131.
- Richardson, D.C., Walsh, K.J., 2006. Binary minor planets. *Annu. Rev. Earth Planet. Sci.* 34 (May), 47–81.
- Rossi, A., Marzari, F., Scheeres, D.J., 2009. Computing the effects of YORP on the spin rate distribution of the NEO population. *Icarus* 202 (July), 95–103.
- Scheeres, D.J., 2007. Rotational fission of contact binary asteroids. *Icarus* 189 (August), 370–385.
- Scheeres, D.J., Gaskell, R.W., 2008. Effect of density inhomogeneity on YORP: The case of Itokawa. *Icarus* 198 (November), 125–129.
- Statler, T.S., 2009. Extreme sensitivity of the YORP effect to small-scale topography. *Icarus* 202 (August), 502–513.
- Stellingwerf, R.F., 1978. Period determination using phase dispersion minimization. *Astrophys. J.* 224 (September), 953–960.
- Walsh, K.J., Richardson, D.C., Michel, P., 2008. Rotational breakup as the origin of small binary asteroids. *Nature* 454 (July), 188–191.
- Warner, B.D., 2009. Asteroid lightcurve analysis at the palmer divide observatory: 2008 September–December. *Minor Planet Bull.* 36 (April), 70–73.
- Warner, B.D., Harris, A.W., Pravec, P., 2009. The asteroid lightcurve database. *Icarus* 202 (July), 134–146.
- Whiteley, R.J., Tholen, D.J., Hergenrother, C.W., 2000. Lightcurve analysis of 4 new monolithic fast-rotating asteroids. *Bull. Am. Astron. Soc.* 32, 1003.